Sustainable Energy & Fuels

Effect of synthesis pH and EDTA on iron hexacyanoferrate for sodium-ion batteries

Journal:	*Sustainable Energy & Fuels*
Manuscript ID	SE-ART-01-2020-000120.R1
Article Type:	Paper
Date Submitted by the Author:	20-Mar-2020
Complete List of Authors:	Neale, Zachary; University of Washington, Materials Science and Engineering Liu, Chaofeng; University of Washington, Materials Science and Engineering Cao, Guo-Zhong ; University of Washington, Materials Science and Engineering

Effect of synthesis pH and EDTA on iron hexacyanoferrate for sodium-ion batteries

Zachary G. Neale[a], Chaofeng Liu[a], and Guozhong Cao[a,*]

[a] Department of Materials Science and Engineering, University of Washington, Seattle, WA 98195, USA

*Corresponding Author:

Prof. Guozhong Cao, email: gzcao@uw.edu

Abstract

Iron hexacyanoferrate (FeHCF) particles were synthesized at room temperature with ethylenediaminetetraacetic acid (EDTA) at varying pH. The presence of EDTA produced faceted particles and increasing synthesis pH resulted in slower reaction kinetics and larger particles with lower water content and fewer anion vacancies determined by TGA and Mössbauer spectroscopy. Electrochemical testing of sodium metal half cells revealed higher capacity in FeHCF particles grown at lower pH with EDTA, obtaining a maximum discharge capacity of 151 mAh/g with 79% capacity retention after 100 cycles at 100 mA/g and a rate capability of 122 mAh/g at 3.2 A/g. In contrast, particles grown at higher pH had stunted low-spin Fe redox activity but with improved long-term cyclic stability. These findings demonstrate that small changes in synthesis pH can greatly affect the growth and electrochemical properties of FeHCF when using a pH sensitive chelating agent such as EDTA.

1. Introduction

The production of high energy density lithium-ion batteries (LIBs) has rapidly increased with growing demand for electric vehicles, portable consumer electronics, and renewable energy production. However, supply-chain sensitivity of lithium, cobalt, and nickel resources puts LIBs at risk for significant price fluctuations and material shortages in the future [1]. For this reason, sodium-ion batteries (SIBs) have been of much investigation as a substitute for LIBs. Despite having lower energy density, SIBs could potentially provide economic advantages over LIBs due to its more earth-abundant supply of precursors and could be more suitable for niche applications such as stationary energy storage systems [2]. Prussian blue (PB) and its analogs (PBAs) have been widely investigated as a suitable SIB cathode material because of its high theoretical capacity, high sodium-ion diffusion, easy synthesis scalability, and readily-available, low-cost precursors [3]. However, actual capacity and cyclic stability of Fe-based PB must still be improved in order for SIBs to become competitive commercially [4].

Prussian blue, chemically known as iron hexacyanoferrate (FeHCF), has the general chemical formula $A_xFe[Fe(CN)_6]_{1-y}\cdot nH_2O$ where *A* represents a variety of possible interstitial cations introduced during synthesis or through electrochemical intercalation [5]. FeHCF typically arranges in a face-centered cubic crystal lattice of Fe cations octahedrally coordinated to the nitrogen of $Fe(CN)_6$ anion octahedra and *A* cations located in the large interstitial sites [6]. The strong ligand field of the cyanide ion results in the C-coordinated Fe cation of $Fe(CN)_6$ groups to take the low-spin electronic configuration while the N-coordinated Fe cation remains in the high-spin state [7]. Consequently, there exists separate redox potentials for high-spin and low-spin Fe whose redox potential may also depend on the amount of water and intercalation site of sodium ions [8, 9, 10].

In general, there are two routes to chemically synthesizing FeHCF. First is through a co-precipitation method, utilizing an iron salt and ferrocyanide salt. The precipitation reaction at room temperature between free iron ions and ferrocyanide complex is rapid, resulting in nanoparticles with poor crystallinity, high vacancies, and high water content [11]. In contrast, high quality FeHCF crystals can be grown through hydrothermal synthesis in which a single precursor, such as sodium ferrocyanide salt, is slowly decomposed in an acidic solution at high temperature to produce free iron ions that can react with undecomposed ferrocyanide ions [11, 12, 13]. This route produces highly crystalline FeHCF particles that have improved capacity and cyclability compared to nanoparticles prepared by simple mixing [11]. However, the one-pot synthesis route creates hazardous cyanide as a byproduct, generating up to six moles of cyanide per mole of FeHCF [14]. Furthermore, this route does not easily allow for the doping or substitution of the *M* species with other transition metals due to the fast precipitation between ferrocyanide and transition metal ions. Therefore, it is important to investigate alternative synthesis routes that avoid cyanide generation and can allow *M* species substitution at room temperature while retaining a highly crystalline structure.

The addition of citrate to the co-precipitation method has been shown to produce cubic crystals of FeHCF, Ni/MnHCF, and CoHCF with improved capacity and cyclic performance for Na-ion batteries [15, 9, 16, 17]. Other chelating agents and their dependence on solution pH have not been studied for their influence on particle growth and electrochemical properties of FeHCF. The following research investigates the effect ethylenediaminetetraacetic acid (EDTA) under different synthesis pH has on the crystal growth and electrochemical properties of FeHCF. EDTA is a hexadentate chelating agent commonly used in industry to suppress the activity of metal ions in solution and is a strong chelator of Fe ions [18]. It forms complexes with metal ions through two amine groups and four carboxyl groups. Due to the pH dependence of carboxyl deprotonation, the solution pH affects the chelation strength of EDTA, thus affecting particle growth and electrochemical performance of FeHCF.

2. Experimental

Synthesis of FeHCF with EDTA at different pH. Separate 0.3 M acetate buffer solutions were made at pH 3.8, 4.0, 4.2, and 4.4 with sodium acetate and acetic acid. Each buffer solution was used to prepare a 200 mL solution of 20 mM $Na_4Fe(CN)_6 \cdot 10H_2O$ and a 200 mL solution of 30 mM $FeCl_2 \cdot 4H_2O$ and 30 mM ethylenediaminetetraacetic acid tetrasodium salt (EDTA). The $FeCl_2$ solution was quickly added to the former solution and stirred for 24 hours at room temperature before particles were collected and washed with water and ethanol through centrifugation. The blue product was dried in air at 80^oC overnight. Herein samples will be labeled as PB(3.8), PB(4.0), PB(4.2) and PB(4.4) corresponding to their respective solution pH during synthesis.

Physical Characterization. The crystal structures of the as-synthesized products were determined via powder X-ray diffraction (XRD) on a Bruker D8 Discover using a Cu-K X-ray source with nickel filter and 1-dimensional X-ray transducer. A JSM 7000F scanning electron microscope was used in SEI mode to collect electron micrographs. SEM samples were prepared by drop casting FeHCF-water suspensions onto silicon substrates and drying at 80 ^oC under vacuum. The optical absorbance spectra were measured with a UV-visible light spectrometer on samples suspended in water, and the optical absorbance at 700 nm was measured for PB(3.8) and PB(4.4) at 10 second intervals for the first 30 minutes after mixing precursor solutions together. Thermal gravimetric analysis (TGA) was performed on samples under nitrogen gas at 5^oC/min. Exhaust gas from TGA was filtered through a 0.1M ferrous sulfate water trap to capture any cyanide gas generated. Mössbauer spectroscopy was performed on FeHCF powders using a ^{57}Co radioactive source.

Electrochemical Characterization. Electrodes were made on aluminum foil by doctor blading a slurry of 70% active material, 20% Super P conductive carbon, and 10% sodium carboxymethylcellulose (CMC) binder dissolved in water and allowed to dry at 80^{o}C under vacuum for 12 hours. 2032 type coin cells were made in an Argon glovebox with a sodium metal anode and Whatman glass fiber separator saturated with 1M $NaClO_4$ in propylene carbonate (PC) with 5 vol% fluoroethylene carbonate (FEC) electrolyte solution. Batteries for cyclic voltammetry did not include FEC additive in their electrolyte. Galvanostatic cycling was done on a LAND battery tester between 2 and 4.3 V. Cyclic voltammetry was performed with an Arbin electrochemical tester between 2 and 4.3 V at 0.1mV/s.

3. Results and discussion

Physical characterization. The XRD patterns of the four FeHCF samples synthesized under different pH match the cubic $Fm\bar{3}m$ crystal structure of Prussian blue (Figure 1). Sharp diffraction peaks suggest large crystallite size with good crystallinity, and diffraction peak intensity increases slightly with synthesis pH. SEM micrographs (Figure 2) show that particles display faceted morphology and particle size increases at higher pH. Particle geometry is not necessarily cubic and consists of irregular particles with square and rectangular facets. The thermodynamic equilibrium shape of FeHCF is cubic because of its face-center-cubic lattice. The synthesized FeHCF particles with EDTA do display faceted features, which might suggest that the crystal was grown under thermodynamic conditions; however, the non-uniformity and irregularity of particle geometry could be due to non-classical crystallization, such as mesocrystal assembly. Mesocrystals are hierarchical structures formed by the oriented self-assembly and fusing of smaller nanoparticles [19, 20, 21]. There are several reports on the formation of FeHCF mesocrystals of various morphologies through hydrothermal synthesis with different organic additives such as glucose, polyethylene glycol, or polyvinylpyrrolidone [22, 23, 24]. The addition of EDTA could assist in oriented aggregation of FeHCF nanocrystals as it has been shown in the formation of biomineral mesocrystal materials [25, 26]. The difference in mesocrystal size between PB(3.8) and PB(4.4) may be due to a difference in the initial nanocrystal size as illustrated in Figure 3.

Crystal size is dependent on the competition between growth rate and nucleation rate, where the energy barrier for nucleation is related to particle solubility and free ion concentration [27]. The solubility product of Prussian blue has been reported as between 10^{-264} and 10^{-177}, resulting in extremely fast nucleation [28]. The presence of EDTA reduces the activity of free Fe in solution by forming a complex with Fe ions, slowing the kinetics of nucleation which typically dominate over particle growth. Formation of crystal nuclei with $[Fe(CN)_6]^{4-}$ anions is more inhibited by EDTA at higher pH, resulting in increased crystal size. Acetate anions from the acetate buffer solution can also form a complex with Fe ions in solution; however, it is a monodentate ligand and has a lower stability constant of $10^{3.2}$ (K_1) compared to $10^{14.3}$ for EDTA [29]. In comparison, FeHCF grown by the same procedure without EDTA results in nanoparticles that do not show any significant difference in particle size between different pH (Figure S1).

UV-visible light spectroscopy of FeHCF particles dispersed in water show an absorbance peak associated with Prussian blue (Figure 4a) at 700 nm. Visible light absorption is due to charge transfer between low-spin Fe^{2+} and high-spin Fe^{3+} ions in Prussian blue [30]. Increasing synthesis pH results in decreasing absorbance at 700 nm but increasing absorbance near 400 nm. The lower absorbance at 700 nm could be caused by an increased concentration of reduced high-spin Fe^{2+} in the larger FeHCF particles. The reduced state of FeHCF, known as Prussian white, is not stable in air and will gradually oxidize to Prussian blue. PB(4.4) may be less prone to oxidation due to its larger particle size, or perhaps because free Fe^{3+} ions in solution are preferentially chelated by EDTA compared to Fe^{2+} [18]. The higher concentration of Fe^{2+} could be balanced by an increased concentration of Na^+ in the FeHCF crystal to maintain charge neutrality. Energy dispersive X-ray spectroscopy (EDS) reveals Na:Fe ratios of 0.39, 0.42, 0.43, and 0.51 for PB(3.8), PB(4.0), PB(4.2), and PB(4.4), respectively. The increasing concentration of Na^+ with synthesis pH for FeHCF samples could directly correspond with the ratio of Fe^{2+} to Fe^{3+} and corroborates the decreasing peak intensity of UV-vis.

The claim that EDTA retards the nucleation of FeHCF particles more at higher pH was tested by measuring optical absorbance at 700 nm during the first 30 minutes of synthesis for PB(3.8) and PB(4.4) (Figure 4b). The solution synthesized at pH 3.8 reaches saturated optical absorbance within the first few minutes of reaction. In contrast, the sample synthesized at pH 4.4 increases optical absorbance more gradually with time, indicating slower precipitation of particles.

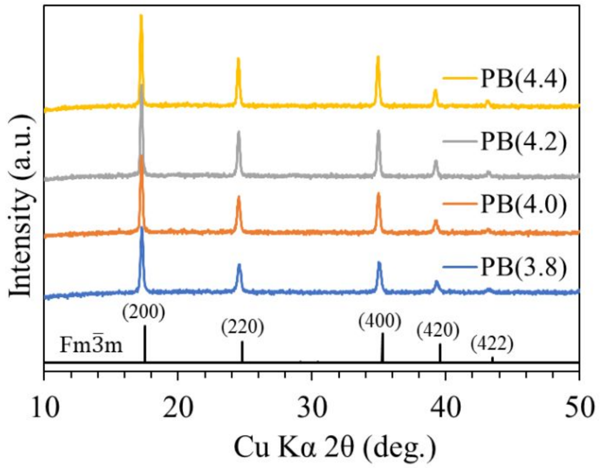

Figure 1. XRD patterns of FeHCF samples between 10-50 degrees compared against ICDD No. 00-052-1907 for Prussian blue.

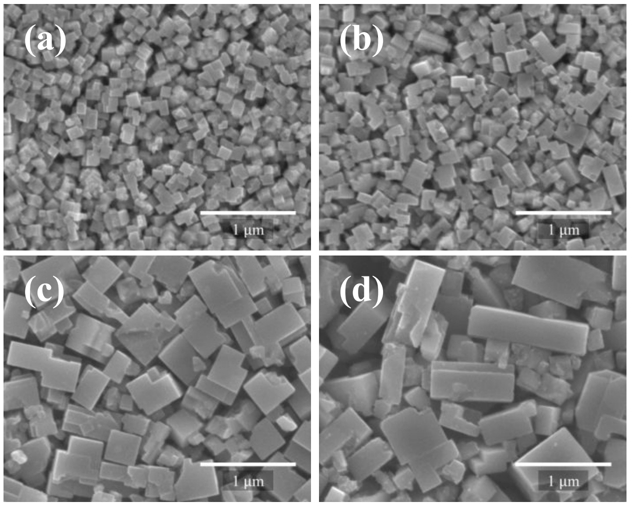

Figure 2. SEM micrographs of (a) PB(3.8), (b) PB(4.0), (c) PB(4.2), and (d) PB(4.4). Scalebar is 1 μm.

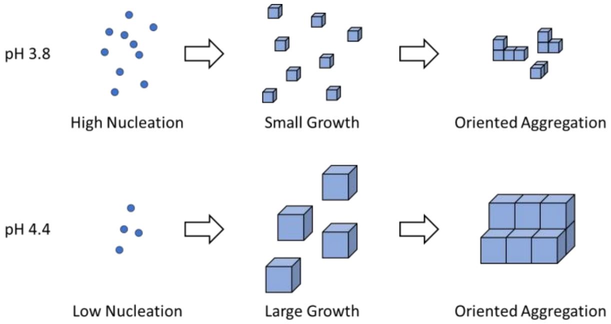

Figure 3. Proposed mechanism of oriented aggregation between different synthesis pH.

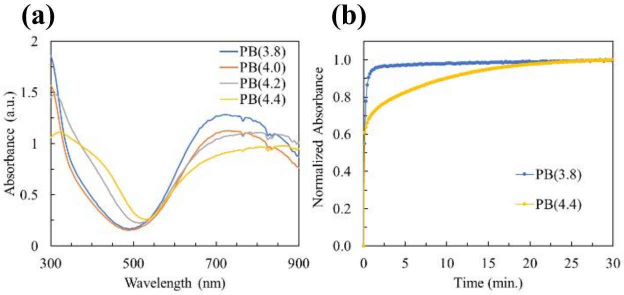

Figure 4. UV-visible light absorbance spectra for FeHCF samples (a). Normalized optical absorbance at 700nm during the first 30 minutes of synthesis (b).

The crystal structure of FeHCF is typically associated with zeolitic water and water coordinated to high-spin Fe in place of $Fe(CN)_6$ anion vacancies. TGA results (Figure 5) show two weight loss regions that corresponding to dehydration and partial decomposition of cyanide groups [31]. The initial weight loss step associated with total dehydration reveals water content of 16.4, 14.4, 13.8, and 13.4 wt% for PB(3.8), PB(4.0), PB(4.2), and PB(4.4), respectively. The increasing water content at lower synthesis pH could be attributed to additional water present in $Fe(CN)_6$ anion vacancy sites and from increased surface absorbed water due to smaller particle size. Additionally, Fe ions in solution are coordinated by water during a typical synthesis which could lead to a high water content of FeHCF during rapid precipitation. When EDTA is added it blocks coordinated water by chelating with Fe ions. At higher pH the chelation strength of EDTA is stronger and more water may be blocked from coordinating with Fe. Furthermore, the dehydration and decomposition temperature increase with particle size which could be due to a thermal delay dependent on particle size, a similar phenomenon to a shift in onset temperature when heating rate is increased.

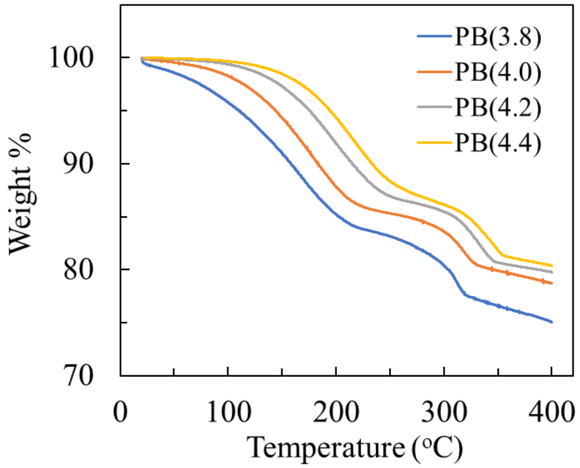

Figure 5. TGA under nitrogen gas at 5°C/min for FeHCF samples.

Mössbauer spectroscopy was performed on PB(3.8) and PB(4.4) to investigate the effect synthesis pH had on $Fe(CN)_6$ vacancies. The nuclear resonance of ^{57}Fe atoms in FeHCF are sensitive to their local chemical environment and valence state. The Mössbauer spectra of PB(3.8) and PB(4.4) (Figure 6) can be fitted with Lorentzian curves representing each iron species and the area of the curve is proportional to the molar fraction of that species. Using the same fitting methodology as Grandjean et al., a single doublet was assigned to low-spin Fe^{2+}, and three doublets were assigned to high-spin Fe^{3+} and Fe^{2+} with their line widths, Γ, held equal to that of the α-Fe calibration of 0.34 mm/s [32]. This is because the presence of low-spin $Fe(CN)_6$ vacancies create several chemically unique identities of high-spin Fe. For PB(4.4) it was necessary to add an additional set of doublets corresponding to high-spin Fe^{2+} to fit a shoulder peak, which corroborates the increased Na:Fe ratio from EDS and decreased absorption peak at 700 nm observed in Figure 4 indicating increased high-spin Fe^{2+} concentration. The fitting parameters of each curve are listed in Table S1.

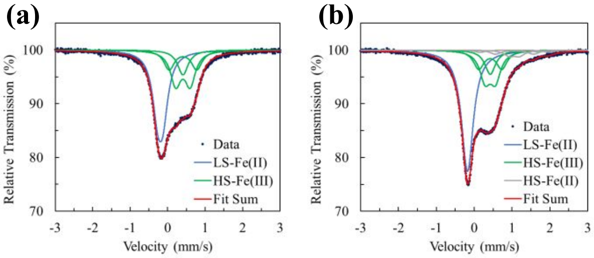

Figure 6. Mössbauer spectra at room temperature of (a) PB(3.8) and (b) PB(4.4) with fitted Lorentzian curves representing iron species.

The curve area ratios between low-spin and high-spin iron species reveal approximately 18 and 4% $Fe(CN)_6$ anion vacancies for PB(3.8) and PB(4.4), respectively, corresponding to estimated chemical formulae of $Na_{0.71}Fe[Fe(CN)_6]_{0.82}\cdot 2.68H_2O$ and $Na_{1.00}Fe[Fe(CN)_6]_{0.96}\cdot 2.38H_2O$ when incorporating EDS and TGA results. This result is supported by the decrease in weighted quadrupole splitting, $\langle \Delta E_Q \rangle$, of high-spin Fe^{3+} from 0.14 to 0.11 mm/s. Quadrupole splitting of the iron nucleus is caused by an electric field gradient contributed to by nonsymmetric valence electrons or ligands [33]. The smaller quadrupole splitting of PB(4.4) suggests its high-spin Fe^{3+} centers are surrounded by a more symmetric octahedra of $Fe(CN)_6$ anions due to fewer vacancies.

Similarly, the isomer shift, δ, of high-spin Fe^{3+} increases from 0.41 to 0.42 mm/s for PB(3.8) and PB(4.4), respectively. The isomer shift is sensitive to *s*-electron density, with more negative shift for increasing *s*-electron density at the nucleus of Fe atoms [34]. High-spin Fe^{3+} in FeHCF are octahedrally coordinated to the electronegative nitrogen of $Fe(CN)_6$, pulling electrons away from its center. When $Fe(CN)_6$ ligands are vacant the *s*-electron density at the nucleus of high-spin Fe increases resulting in a less positive isomer shift as seen in PB(3.8). The decreasing vacancy concentration of FeHCF grown with EDTA at higher pH indicated by Mössbauer spectroscopy may be attributed to the slower nucleation and growth rate of particles.

Electrochemical results. Cyclic voltammetry (CV) of sodium metal half-cells reveals several redox peaks corresponding to sodium ion intercalation and deintercalation (Figure 7). The redox potential of sodium-ion intercalation into FeHCF can be affected by ligand field energy of the transition metal ion and energy of the intercalation site which could be influenced by the concentration of sodium and water in the crystal [35]. Previous studies have modeled the different energies associated with ion intercalation into different sites, as well as the influence of water molecules. Possible sodium sites include 8c (body-centered), 24d (face-centered), 32f (displaced 8c towards high-spin Fe), 32f’ (displaced 8c towards low-spin Fe), and 48g (displaced between 8c and 24d) [35]. Additionally the presence of water has been reported to affect the redox potential of sodium ion intercalation in the large interstitial sites of FeHCF [10, 36].

Cyclic voltammetry during the initial charge cycle shows a large current response at high-voltage which may be the oxidation of water in the crystal. The oxidation peak is larger in PB(3.8) than

PB(4.4) which could be because of the larger water content of PB(3.8). The first reduction peak located above 3.5 V may be the intercalation of Na-ions into hydrated sites and low-spin Fe reduction [12]. This peak's redox potential is higher for PB(3.8) than PB(4.4) which could be due to the amount of water, which has been modeled to influence the redox potential of FeHCF and decrease in potential with lowering water content [10]. After subsequent cycling the first reduction peak above 3.5 V decreases in current density while the second reduction peak at around 3.3V increases, attributed to dehydrated Na-ion intercalation and low-spin Fe reduction. The reduction and oxidation peaks below this voltage are attributed to Na-ion intercalation and high-spin Fe reduction. The several peaks of high-spin Fe may also be due to the influence of water and intercalation site preference.

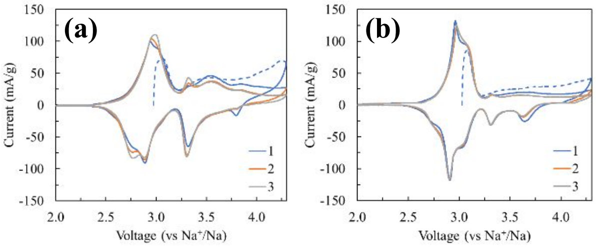

Figure 7. Cyclic voltammetry at 0.1 mV/s for PB(3.8) (a) and PB(4.4) (b). Dashed line is initial charge.

Galvanostatic cycling was performed on sodium metal half cells at 100 mA/g (Figure 8). During the initial charge cycle PB(4.4) shows a significantly larger plateau at 3.1 V than PB(3.8) indicating a greater concentration of initial high-spin Fe^{2+}. This corroborates the presence of a high-spin Fe^{2+} peak in the Mössbauer spectra and lower absorbance at 700 nm in UV-Vis of PB(4.4). On the other hand, the initial charge capacity contribution beyond this voltage plateau is larger for PB(3.8), indicating more redox active low-spin $[Fe(CN)_6]^{4-}$ despite having slightly more vacancies according to Mössbauer spectroscopy. The first cycle discharge capacities were 151, 142, 125, and 124 mAh/g for PB(3.8), PB(4.0), PB(4.2) and PB(4.4), respectively. The increased capacity of

FeHCF synthesized at lower pH with EDTA is primarily due to a larger contribution of low-spin Fe redox activity (Figure S4). When the synthesis of FeHCF is carried out without EDTA, there is no significant difference in capacity or voltage between pH 3.8 and pH 4.4 (Figure S5), confirming that the difference is primarily influenced by the addition of EDTA and not the acetate buffer at different pH.

Capacity loss occurs after the first cycle and is more significant in samples synthesized at higher pH. Capacity loss could arise from irreversible ion insertion or extraction, structural collapse due to crystal distortion or dehydration, and irreversible side-reactions. Work by Rudola, et al. on high-quality micron-sized FeHCF crystals demonstrate electrochemical dehydration of the crystal when cycled to 4.3 V which may result in structural distortion and capacity loss [12]. PB(4.4) shows a larger initial capacity loss despite having slightly less water than PB(3.8). The larger particle size of PB(4.4) with fewer vacancies may be less accommodating to structural transformation resulting in larger initial capacity loss. Upon further cycling all FeHCF samples suffer from capacity decay at different severity (Figure 9) with samples synthesized at higher pH demonstrating better cyclic performance. Capacity retention up to 100 cycles after the 3rd cycle was 82, 85, 94, and 91% and average coulombic efficiencies (discharge divided by charge) were 99.2, 99.5, 99.5, and 99.6% for PB(3.8), PB(4.0), PB(4.2), and PB(4.4), respectively. Long term cyclic instability in FeHCF can be caused by lattice collapse from $Fe(CN)_6$ vacancies and side-reactions from the oxidation of coordinated water [37], thus the samples grown at higher pH with a more perfect crystal structure and less water has improved cyclability.

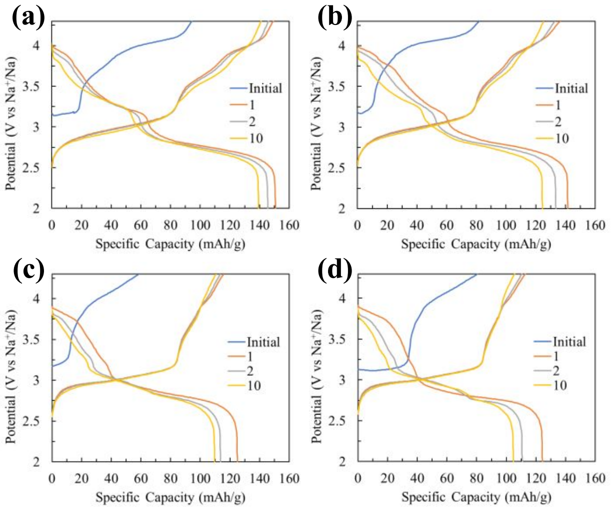

Figure 8. Galvanostatic profile at 100 mA/g of the initial charge and subsequent cycles for FeHCF synthesized with EDTA at pH 3.8 (a), pH 4.0 (b), pH 4.2 (c), and pH 4.4 (d).

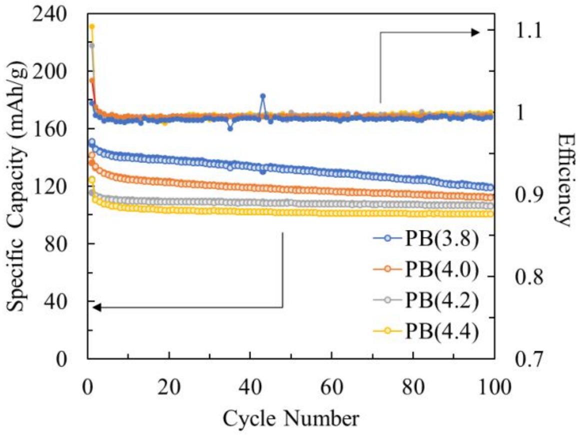

Figure 9. Galvanostatic cycling at 100 mA/g. Discharge shown as open circles and charge shown as filled circles.

The intercalation kinetics of FeHCF samples were investigated by cycling batteries at various current densities (Figure 10). The specific discharge capacities at a current density of 3.2 A/g were 120, 104, 95, and 89 mAh/g, corresponding to capacity retentions of 84, 80, 83, and 80% respectively for PB(3.8), PB(4.0), PB(4.2), and PB(4.4) compared to their 4th cycle at 100 mA/g. The high capacity retention at high current indicates fast intercalation kinetics which can be ascribed to Prussian Blue's unique cage-like structure which can facilitate rapid ion transport. However, further analysis of discharge curves of PB(3.8) and PB(4.4) when current rate increases shows that capacity of the upper voltage plateau attributed to low-spin Fe is disproportionately lost compared to the lower voltage plateau attributed to high-spin Fe (Figure 11). The asymmetric decrease in capacity between voltage plateaus suggests that the intercalation or redox mechanism of the upper plateau is more impacted by kinetics. Furthermore, the capacity retention of the upper voltage plateau more quickly decreases for the larger microscale particles of PB(4.4) retaining about 32% capacity compared to 61% for PB(3.8) at 3.2 A/g (Figure S7). In contrast, the lower voltage plateau capacity retains about 97% capacity for PB(4.4) and there is no decrease for PB(3.8). The larger diffusion distance of micrometer-sized particles could be responsible for the decreased electrochemical activity of larger particles grown at higher pH with EDTA, despite having fewer vacancies.

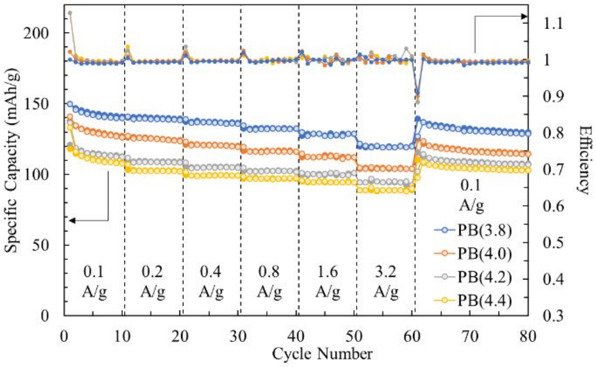

Figure 10. Galvanostatic cycling at various current rates. Discharge shown as open circles and charge shown as filled circles.

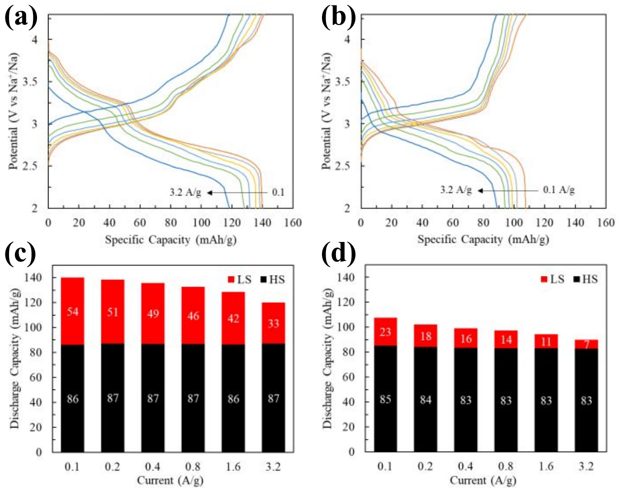

Figure 11. Rate performance of PB(3.8) (a) and PB(4.4) (b), and their respective estimated capacity contributions between low-spin and high-spin Fe (c, d).

4. Conclusions

The effect synthesis pH and EDTA had on FeHCF growth and its influence on sodium ion battery performance was investigated. Increasing synthesis pH results in slower nucleation kinetics leading to increased particle size, fewer anion vacancies, and decreased water content. However, galvanostatic cycling illustrated that FeHCF synthesized with EDTA at lower pH had increased capacity with more prevalent low-spin Fe redox activity and increased rate performance, but also suffered from faster cyclic decay.

It was originally hypothesized that particles with fewer vacancies would have improved capacity. While this still may be possible, rate-dependent results illustrate that any gains in capacity because of fewer vacancies were overshadowed by kinetic limitations of the low-spin Fe redox reaction. In summary, growth of FeHCF faceted particles with EDTA can be controlled by the adjustment of synthesis pH that results in significant changes in their electrochemical activity over a small pH range. These findings suggest that pH should be carefully considered especially when utilizing a chelating agent in other procedures of FeHCF synthesis.

5. Conflicts of Interest

There are no conflicts to declare.

6. Acknowledgements

This work was supported in part by the National Science Foundation (DMR 1505902 and CBET-1803256). The first author appreciates Dr. David Pengra and the UW Physics department for their assistance with Mössbauer spectroscopy.

References

[1] C. Vaalma, D. Buchholz, M. Weil and S. Passerini, "A cost and resource analysis of sodium-ion batteries," *Nature Reviews Materials,* vol. 3, p. 18013, 2018.

[2] J. F. Peters, A. P. Cruz and M. Weil, "Exploring the Economic Potential of Sodium-Ion Batteries," *Batteries,* vol. 5, no. 10, 2019.

[3] J. Qian, C. Wu, Y. Cao, Z. Ma, Y. Huang, X. Ai and H. Yang, "Prussian Blue Cathode Materials for Sodium-Ion Batteries and Other Ion Batteries," *Advanced Energy Materials,* vol. 8, no. 17, p. 1702619, 2018.

[4] Q. Liu, Z. Hu, M. Chen, C. Zou, H. Jin, S. Wang, S.-L. Chou, Y. Liu and S.-X. Dou, "The Cathode Choice for Commercialization of Sodium-Ion Batteries: Layered Transition Metal Oxides versus Prussian Blue Analogs," *Advanced Functional Materials,* p. 1909530, 2020.

[5] Y. Xu, S. Zheng, H. Tang, X. Guo, H. Xue and H. Pang, "Prussian blue and its derivatives as electrode materials for electrochemical energy storage," *Energy Storage Materials,* vol. 9, pp. 11-30, 2017.

[6] M. B. Zakaria and T. Chikyow, "Recent advances in Prussian blue and Prussian blue analogues: synthesis and thermal treatments," *Coordination Chemistry Reviews,* vol. 352, pp. 328-345, 2017.

[7] A. Kumar and S. M. Yusuf, "Structural and magnetic properties of Fe[Fe(CN)6]*4H2O," *Physical Review B,* no. 71, 2005.

[8] Y. Lu, L. Wang, J. Cheng and J. B. Goodenough, "Prussian blue: a new framework of electrode materials for sodium batteries," *Chemical Communications,* no. 48, pp. 6544-6546, 2012.

[9] C. Yan, A. Zhao, F. Zhong, X. Feng, W. Chen, J. Qian, X. Ai, H. Yang and Y. Cao, "A low-defect and Na-enriched Prussian blue lattice with ultralong cycle life for sodium-ion battery cathode," *Electrochimica Acta,* p. 135533, 2020.

[10] X. Guo, Z. Wang, Z. Deng, X. Li, B. Wang, X. Chen and S. P. Ong, "Water Contributes to Higher Energy Density and Cycling Stability of Prussian Blue Analogue Cathodes for Aqueous Sodium-Ion Batteries," *Chemistry of Materials,* vol. 31, pp. 5933-5942, 2019.

[11] Y. You, X.-L. Wu, Y.-X. Yin and Y.-G. Guo, "High-quality Prussian blue crystals as superior cathode materials for room-temperature sodium-ion batteries," *Energy & Environmental Science,* vol. 7, pp. 1643-1647, 2014.

[12] A. Rudola, K. Du and P. Balayaa, "Monoclinic Sodium Iron Hexacyanoferrate Cathode and Non-Flammable Glyme-Based Electrolyte for Inexpensive Sodium-Ion Batteries," *Journal of The Electrochemical Society,* vol. 164, no. 6, pp. A1098-A1109, 2017.

[13] D. Cai, X. Yang, B. Qu and T. Wang, "Comparison of the electrochemical performance of iron hexacyanoferrate with high and low quality as cathode materials for aqueous sodium-ion batteries," *Chemical Communications,* no. 53, pp. 6780-6783, 2017.

[14] Y. Liu, G. Wei, M. Ma and Y. Qiao, "Role of Acid in Tailoring Prussian Blue as Cathode for High-Performance Sodium-Ion Battery," *Chemistry - A European Journal,* vol. 23, pp. 15991-15996, 2017.

[15] Y. Liu, Y. Qiao, W. Zhang, Z. Li, X. Ji, L. Miao, L. Yuan, X. Hu and Y. Huang, "Sodium storage in Na-rich NaxFeFe(CN)6 nanocubes," *Nano Energy,* vol. 12, pp. 386-393, 2015.

[16] R. Chen, Y. Huang, M. Xie, Z. Wang, Y. Ye, L. Li and F. Wu, "Chemical Inhibition Method to Synthesize Highly Crystalline Prussian Blue Analogs for Sodium-Ion Battery Cathodes," *Applied Materials and Interfaces,* vol. 8, p. 31669−31676, 2016.

[17] F. Shiba, R. Fujishiro, T. Kojima and Y. Okawa, "Preparation of Monodisperse Cobalt(II) Hexacyanoferrate(III) Nanoparticles Using Cobalt Ions Released from a Citrate Complex," *The Journal of Physical Chemistry C,* vol. 116, pp. 3394-3399, 2012.

[18] A. E. Martell, R. J. Motekaitis, D. Chen, R. D. Hancock and D. McManus, "Selection of new Fe(lll)/Fe(ll) chelating agents as catalysts for the oxidation of hydrogen sulfide to sulfur by air," *Canadian Journal of Chemistry,* vol. 74, no. 10, pp. 1872-1879, 1996.

[19] E. Uchaker and G. Cao, "Mesocrystals as electrode materials for lithium-ion batteries," *Nano Today,* vol. 9, no. 4, pp. 499-524, 2014.

[20] E. V. Sturm and H. Cölfen, "Mesocrystals: structural and morphogenetic aspects," *Chemical Society Reviews,* vol. 45, no. 21, pp. 5821-5833, 2016.

[21] C. Liu, C. Zhang, H. Song, C. Zhang, Y. Liu, X. Nan and G. Cao, "Mesocrystal MnO cubes as anode for Li-ion capacitors," *Nano Energy,* vol. 22, pp. 290-300, 2016.

[22] M. Hu, J.-S. Jiang, C.-C. Lin and Y. Zeng, "Prussian blue mesocrystals: an example of self-construction," *CrystEngComm,* vol. 12, pp. 2679-2683, 2010.

[23] X.-J. Zheng, Q. Kuang, T. Xu, Z.-Y. Jiang, S.-H. Zhang, Z.-X. Xie, R.-B. Huang and L.-S. Zheng, "Growth of Prussian Blue Microcubes under a Hydrothermal Condition: Possible Nonclassical Crystallization by a Mesoscale Self-Assembly," *Journal of Physical Chemistry C,* vol. 111, no. 12, pp. 4499-4502, 2007.

[24] H. Ming, N. L. K. Torad, Y.-D. Chiang, K. C.-W. Wu and Y. Yamauchi, "Size- and shape-controlled synthesis of Prussian Blue nanoparticles by a polyvinylpyrrolidone-assisted crystallization process," *CrystEngComm,* vol. 14, pp. 3387-3396, 2012.

[25] Q. Chen, C. Jia, Y. Li, J. Xu, B. Guan and M. Z. Yates, "α-Calcium Sulfate Hemihydrate Nanorods Synthesis: A Method for Nanoparticle Preparation by Mesocrystallization," *Langmuir,* no. 33, pp. 2362-2369, 2017.

[26] R. Xie, Z. Feng, S. Li and B. Xu, "EDTA-Assisted Self-Assembly of Fluoride-Substituted Hydroxyapatite Coating on Enamel Substrate," *Crystal Growth and Design,* no. 11, pp. 5206-5214, 2011.

[27] J. J. De Yoreo and P. G. Vekilov, "Principles of Crystal Nucleation and Grwoth," *Reviews in Mineralogy and Geochemistry,* vol. 54, no. 1, pp. 57-93, 2003.

[28] R. S. Ghosh, D. A. Dzombak and R. G. Luthy, "Equilibrium precipitation and dissolution of iron cyandie solids in water," *Environmental ENgineering Science,* vol. 16, no. 6, pp. 293-313, 1999.

[29] J. A. Dean, Lange's Handbook of Chemistry, New York, USA: McGraw-Hill, 1985.

[30] L. Samain, F. Grandjean, G. J. Long, P. Martinetto, B. Pierre and D. Strivay, "Relationship between the Synthesis of Prussian Blue Pigments, Their Color, Physical Properties, and Their Behavior in Paint Layers," *The Journal of Physical Chemistry C,* vol. 117, no. 19, pp. 9693-9712, 2013.

[31] C. Aparicio, L. Machala and Z. Marusak, "Thermal decomposition of Prussian blue under inert atmosphere," *Journal of Thermal Analysis and Calorimetry,* vol. 110, pp. 661-669, 2012.

[32] F. Grandjean, L. Samain and G. J. Long, "Characterization and utilization of Prussian Blue and its pigments," *Dalton Transactions,* vol. 45, p. 18018, 2016.

[33] T. L. Greaves and J. D. Cashion, "Site analysis and calculation of the quadrupole splitting of Prussian Blue Mossbauer spectra," *Hyperfine Interact,* vol. 237, no. 70, 2016.

[34] B. Fultz, "Mossbauer Spectrometry," in *Characterization of Materials*, E. Kaufmann, Ed., New York, John Wiley, 2011.

[35] C. Ling, J. Chen and F. Mizuno, "First-Principles Study of Alkali and Alkaline Earth Ion Intercalation in Iron Hexacyanoferrate: The Important Role of Ionic Radius," *The Journal of Physcial Chemistry C,* vol. 117, pp. 21158-21165, 2013.

[36] L. Chen, H. Shao, X. Zhou, G. Liu, J. Jiang and Z. Liu, "Water-mediated cation intercalation of open-framework indium hexacyanoferrate with high voltage and fast kinetics," *Nature Communications,* vol. 7, p. 11982, 2016.

[37] Y. Yang, E. Liu, X. Yan, C. Ma, W. Wen, X.-Z. Liao and Z.-F. Ma, "Influence of Structural Imperfection on Electrochemical Behavior of Prussian Blue Cathode Materials for Sodium Ion Batteries," *Journal of The Electrochemical Society,* vol. 163, no. 9, pp. A2117-A2123, 2016.

[38] H.-M. Yang, J. R. Hwang, D. Y. Lee, K. B. Kim, C. W. Park, H. R. Kim and K.-W. Lee, "Eco-friendly one-pot synthesis of Prussian blue-embedded magnetic hydrogel beads for the removal of cesium from water," *Scientific Reports,* vol. 8, no. 11476, 2018.

[39] M. Gautam, K. Poudel, C. S. Yong and J. O. Kim, "Prussian blue nanoparticles: Synthesis, surface modification, and application in cancer treatment," *International Journal of Pharmaceutics,* vol. 549, no. 1-2, pp. 31-49, 2018.

[40] L. Hedley, L. Porteous, D. Hutson, N. Robertson and J. O. Johansson, "Electrochromic bilayers of Prussian blue and its Cr analogue," *Journal of Materials Chemistry C,* no. 6, pp. 512-517, 2018.

[41] Y. Zeng, G.-F. Chen, Z. Jiang, L.-X. Ding, S. Wang and H. Wang, "Confined heat treatment of a Prussian blue analogue for enhanced electrocatalytic oxygen evolution," *Journal of Materials Chemistry A,* no. 6, pp. 15942-15946, 2018.

[42] Y. Zhang, B. Huang, F. Yu, Q. Yuan, M. Gu, J. Ji, Y. Zhang and Y. Li, "3D nitrogen-doped graphite foam@Prussian blue: an electrochemical sensing platform for highly sensitive determination of H2O2 and glucose," *Microchimica Acta,* vol. 185, no. 86, 2018.

[43] B. Wang, Y. Han, X. Wang, N. Bahlawane, H. Pan, M. Yan and Y. Jiang, "Prussian Blue Analogs for Rechargeable Batteries," *iScience,* vol. 3, pp. 110-133, 2018.

[44] H. Fu, C. Liu, C. Zhang, W. Ma, K. Wang, Z. Li, X. Lu and G. Cao, "Enhanced storage of sodium ions in Prussian blue cathode materials through nickel doping," *Journal of Materials Chemistry A,* vol. 5, p. 9604, 2017.

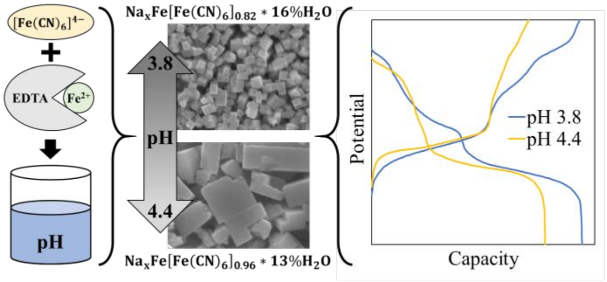

Adjusting synthesis pH of EDTA chelate assisted precipitation of FeHCF affects particle size, vacancies, water content, and redox activity.